Shock Waves (2021) 31:75–88
https://doi.org/10.1007/s00193-020-00983-8

ORIGINAL ARTICLE

Proton radiography of explosively dispersed metal particles with varying volume fraction and varying carrier phase

K. T. Hughes[1] · J. J. Charonko[1] · K. P. Prestridge[1] · N. H. Kim[2] · R. T. Haftka[2] · S. Balachandar[2]

Received: 3 April 2020 / Revised: 19 November 2020 / Accepted: 30 November 2020 / Published online: 4 January 2021

Abstract
A series of experiments were performed to provide validation data for explosively driven multiphase flows at moderate-to-high volume fractions. A 13 × 6 mm cylindrical packet of 115-μm steel particles was dispersed explosively. In contrast to shock tube studies, the particles were subjected to a high-Mach-number shock, in the presence of an ambient fluid, and a contact interface between the ambient and the explosive products. The first five experiments lowered the global volume fraction by replacing portions of the particle bed with hollow glass microspheres, dispersing the particles into vacuum. Three global fractions were investigated: 60%, 40%, and 20%. The next five experiments did not lower the volume fraction but instead varied the ambient fluid. Three ambient fluids were investigated: air, xenon, and SF_6. To penetrate the optically opaque explosive products present and track the dispersed particle cloud, proton radiography was performed. The high-volume-fraction cases exhibit a piston-like motion for all ambient conditions, with an increasingly stochastic motion present for the lower volume fractions. Particle fronts extracted from the transmission radiographs exhibit almost constant velocity. Furthermore, centerline particle fronts for the high-volume-fraction cases, with both vacuum and varying ambient gas conditions, were almost the same, suggesting the primary impulse to particle bed motion arises from the contact interface between the ambient and the detonation products. Lower volume fractions were accelerated to higher velocities, behaving as though they were a single object of decreased density being acted on by a force of constant magnitude.

Keywords Proton radiography · Multiphase flow · Shock–particle interaction · Uncertainty quantification

1 Introduction

Compressible multiphase flows are a challenging and rich topic within the fluid mechanics community. Such flows may arise in the natural world in the case of dispersal of particulate from a volcanic eruption or in engineering applications such as the dispersal of particles by ordinance. Large-scale experiments have been performed by Frost et al. [1–4] examining the explosive dispersal of particles in both heterogeneous and stratified explosive-particle mixtures subjected to a detonation wave. The detonation replaces the central explosive with a high-density, high-temperature gas that propagates outward. A shock wave travels through the particle bed, followed by a contact discontinuity between the shocked air and the explosive products. In the early times, the detonation wave causes the particles to collide and compact with each other. As the particles disperse, the experiments observe a series of large-scale jets or fingers that form in the advancing particle front.

Microscale experiments by Sun et al. [5–8] have measured the forces on a single stationary particle subjected to a moderate shock. When comparing the experimental results to drag relations proposed as compressible generalizations of the Maxey–Riley–Gatignol equation [9,10], the generalized force formula captures the magnitude and timing of the peak force quite well [11–13]. However, the extension of these models from a single particle to a shock-driven multiphase instability is still an ongoing area of research [14]. Shock-tube experiments examining the behavior of moving particles have been performed by variety of researchers [15–18]. In these experiments, the position of the particle is observed after being subjected to a shock and the time-varying drag

Communicated by D. Frost.

✉ N. H. Kim
nkim@ufl.edu

[1] P-23, Physics Division, Los Alamos National Laboratory, Los Alamos, NM 87547, USA

[2] Department of Mechanical and Aerospace Engineering, University of Florida, Gainesville, FL 32611, USA

force extracted. Together these microscale experiments provide a wealth of validation data in the modest-Mach-number regime for a single particle for the proposed drag force relations. Hughes et al. [19] extended the validation data for a single particle to the extreme conditions of a particle being subjected to a post-detonation flow, where a particle is subjected both to a high-Mach-number shock and a strong contact discontinuity.

Similar to the investigations of a single particle, other investigations have been performed at the mesoscale where many particles are subjected to a moderate-Mach-number shock. In this regime, not only are the individual drag forces important, but the particles compact and collide with each other as well. However, the flows still lack the strong contact discontinuity present in detonation conditions. Dilute suspensions of particles ($\phi < 1\%$) subjected to a shock have been studied extensively by researchers such as Rudinger [20]. Less common is examination of multiphase flows where moderate-to-large volume fractions are present ($\phi > 5\%$). Wagner et al. [21] examined shock wave impingement on a free-falling particle curtain of approximately 20% volume fraction by tracking the upstream and downstream particle fronts through high-speed schlieren photography. Under very similar experimental conditions, Kellenberger et al. [22] examined the behavior of stationary particle wafers of approximately 48% volume fraction subjected to a shock wave through high-speed photography. Note in these studies the volume fraction is less than the 60% commonly found in particle beds typical for the explosive dispersal of particles [23]. Rodriguez et al. [24] performed investigations of an annular particle bed subjected to a shock within a Hele-Shaw cell and demonstrated the formation of instabilities at even the relatively low Mach numbers investigated. The volume fraction is not reported, but the particles are close packed and likely 40% or greater.

There are three major motivations for the series of experiments presented in this paper. First, the experiments are motivated by the lack of validation data for particle drag force models in the regime of moderate-to-high volume fraction and high-Mach-number flow. Second, the series presented in this paper, conducted at Los Alamos National Laboratory (LANL), were designed to improve upon the earlier unpublished experiments performed at Eglin Air Force Base (AFB). Third, there is a need for a new set of experiments that retain all the physics of the large-scale explosive tests, but on a smaller scale. The large-scale experiments typically contain billions of particles, whereas these mesoscale experiments are limited to less than a million particles. The reduction of particles could provide a reduction in computational burden while still providing validation data within the high-volume-fraction and high-Mach-number flow regime.

The remainder of this paper is organized as follows. Section 2 will briefly discuss a prior experiment performed at Eglin AFB, motivating the need for proton radiography to measure the particle dispersal. Section 3 will detail the setup of the experiments performed at LANL. Section 4 will overview the uncertainty quantification performed of the experimental inputs. The time-varying particle fronts are extracted from the proton radiographs in Sect. 5. From the particle front positions, the particle front velocity may be extracted and compared with the classical and porous Gurney relations. In addition, the time-varying particle packet width is also extracted to provide an additional validation metric. Section 6 concludes the paper with a summary of the work.

2 Previous Eglin AFB experiments

An initial set of unpublished experiments were carried out at Eglin AFB. The experimental setup and diagnostics were almost the same as the experiments presented in detail in Hughes et al. [19], with exceptions in the size of the explosive casing, particles, and amount of explosive. Whereas in Hughes et al. [19] the casing had a 5.1-cm outer diameter, the outer diameter of the explosive casing used in the Eglin AFB experiments was increased to 10.2 cm. The explosive was reduced from three 12.7-mm-by-12.7-mm pellets of PBXN-5 to one. The doubling of the casing outer diameter and the reduction of the amount of explosive used prevented the heavy fragmentation of the casing seen in Hughes et al. [19], significantly reducing uncertainty by preventing venting of the explosive products through the casing. The particles were 100–130-μm tungsten particles instead of relatively large 2-mm particles. To bring the particles in contact with the explosive, 0.5 g of tungsten particles was wrapped in wetted tissue paper and placed within the mouth of the casing.

As in the Hughes et al. [19] experiments, to observe the particle motion X-ray photography was necessary to pierce the opaque explosive products, as shown in Fig. 1. Clustering in the X-ray image suggests that the particle packet was initially non-uniform, giving rise to two jets on the X-ray image with relatively few particles present at the centerline. Additionally, the results reveal an uncertainty present in the diagnostics not present in the Hughes et al. [19] experiments. The particles spread very quickly in the X-ray imagery, such that the particle front locations are difficult to differentiate on the multiple-exposure film. This uncertainty, added to that of the particle packet, degraded the usefulness of the data for validation. Based on these observations, we improved the experiments with a well-characterized bed and a superior diagnostic for measuring the particle front positions, such as proton radiography.

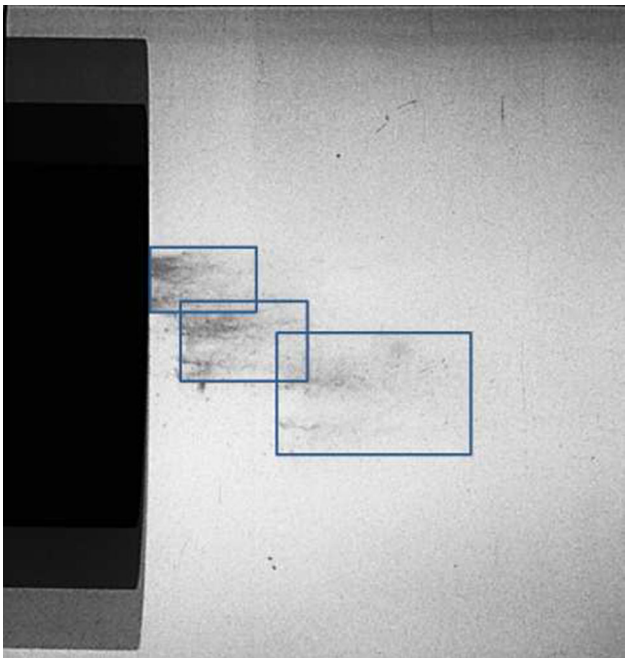

Fig. 1 Sample multiple-exposure X-ray image obtained from the unpublished Eglin AFB experiment. Exposures were taken at 30, 40, and 60 μs after detonation. The blue squares are drawn to demonstrate the relative locations of the particle cloud. The shift in the X-ray images is due to the different orientations of the three X-ray heads

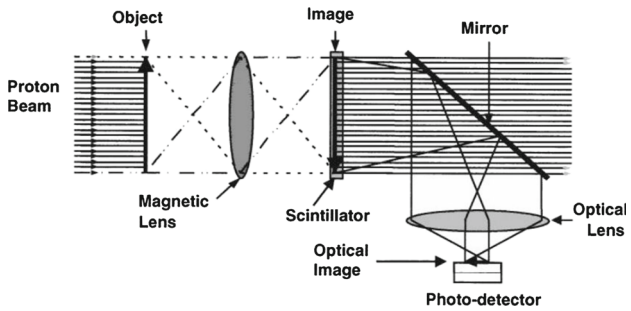

Fig. 2 Proton radiography schematic showing the collimated beam of protons, scintillator, and optical system to capture the radiographs [25]

3 Experimental setup

3.1 Proton radiography diagnostic

The experiments were performed at the Los Alamos Neutron Science Center Proton Radiography facility. Proton radiography utilizes 800-MeV protons provided by a linear particle accelerator [25]. A brief schematic is shown in Fig. 2. A beam of collimated protons is passed through the object of interest. The protons are guided by a series of magnetic lenses to focus the protons on the image plane, where a scintillator converts the protons to photons. The photons are turned out of the beam path with a mirror and passed to the camera group.

Proton radiography is advantageous for this type of dynamic imaging because it has a high depth of penetration [25], and the ability to image through a magnetic lens, allowing for the distal refocus of imaging while correcting for chromatic aberrations, to first order [26]. This distal location of the detector system is ideally suited for imaging high explosive (HE) experiments that pose a risk to detection systems. Additionally, the pulse structure of the LANSCE accelerator allows for arbitrary temporal allocation of frame spacing, combined with a fast detector system that allows for up to 24 frames of acquired dynamic radiography at the LANSCE proton radiography facility, down to 50-ns inter-frame spacing. By employing magnetic lens magnification, spatial resolution scales accordingly, from approximately 200 μm for the identity lens, to 50 μm for the ×3 magnifier [27], to 25 μm for the ×7 magnifier [28] that are available at the LANSCE proton radiography facility.

The protons pierce the opaque explosive products produced during detonation to provide 21 to 24 time-resolved images of the particle fronts. Images were spaced 1–2 μs apart with a resolution of 844 × 853 pixels. A ×3 magnifier is used to provide a 45-mm-by-45-mm field of view with a resolution of 50 μm/pixel. Tests are performed within a 1.83-m-diameter spherical containment vessel that is pumped down to vacuum.

3.2 Varying volume fraction tests

A set of experiments varying the initial volume fraction, designated Shots 1–5, were conducted in October 2017. The test article is shown in Fig. 3. Figure 3a shows a cross section of the casing with the explosive driver used to expel the particles. Figure 3b shows a shot loaded onto the stage that was subsequently lowered into the 1.83-m-diameter spherical containment vessel. U-shaped plastic pieces with steel screws were used to align the casing with the proton beam.

A 10.2-cm-outer-diameter steel casing (AISI 4340) was used with a central bore of 13.1 mm diameter and a depth of 19.1 mm. The reader will note that the explosive train and casing used in the Eglin AFB experiments were matched in the LANL experiments to ensure minimal casing fragmentation occurred (PBXN-5 and PBX-9501 are approximately equivalent). The casing showed minor deformation post-test, but no fragmentation was observed. Examination of post-detonation photographs, as shown in Fig. 4, shows the bore diameter increased from 13.1 to 15 ± 3 mm, an increase of approximately 15%.

A pellet of PBX-9501 (12.7 mm diameter with 12.7 mm length) was initiated by a Teledyne RISI RP-80 exploding bridgewire detonator. When examining Fig. 3a, a slight step is visible along the length of the center bore. The step was necessary to locate the pellet of PBX-9501 exactly and provide a consistent particle bed depth. The PBX-9501 pellet

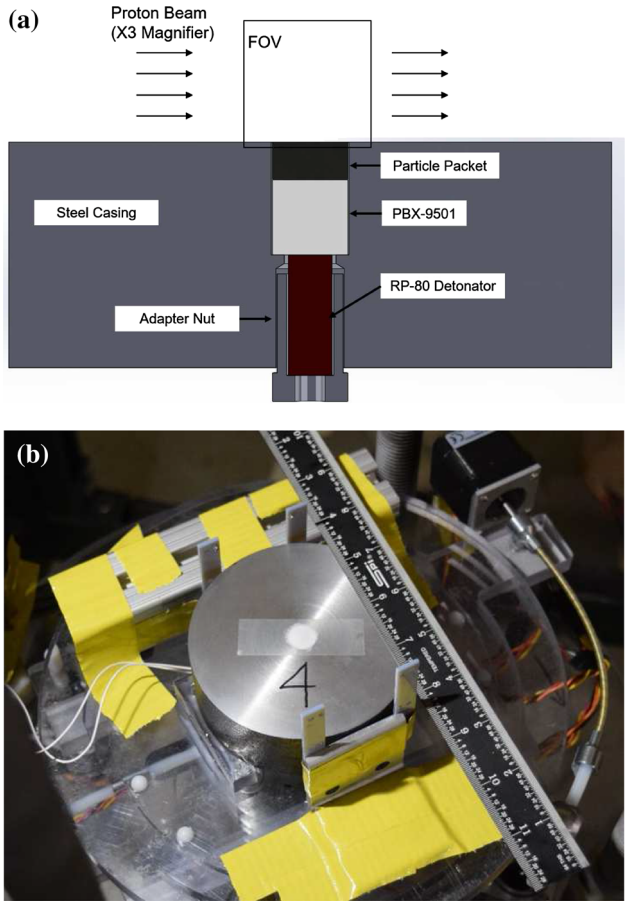

Fig. 3 Details of the test article. **a** Cross-sectional view showing the particle packet and explosive train used in both October 2017 and November 2018 tests. Note the small step used to locate the pellet of PBX-9501. **b** Assembled article for the October 2017 tests on the test stand with alignment fiducials in view

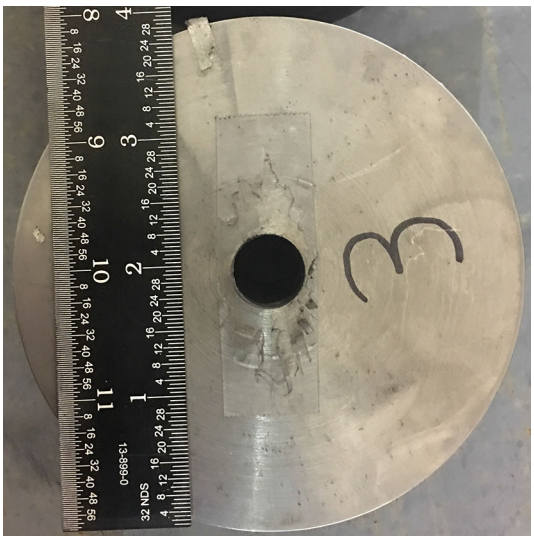

Fig. 4 Post-detonation photograph of the explosive casing

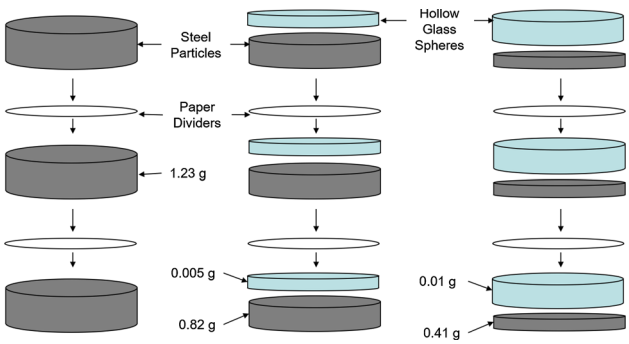

Fig. 5 Details of the three configurations used for the particle packet. The first configuration (left) shows the three layers of steel particles separated by two paper dividers to give a global volume fraction of 60%. The second configuration (middle) replaced 1/3 of the depth of each layer with HGM to give a global volume fraction of 40%. The third configuration (right) replaced 2/3 of the depth of each layer with HGM to give a global volume fraction of 20%

was epoxied to this step using Barcobond to prevent movement of the explosive as the detonator is brought into contact with the explosive using the adapter nut. Time is measured from detonator initiation, determined from a current viewing resistor with approximately $\pm 0.04\,\mu$s uncertainty.

After setting the explosive, a 13.1-mm-diameter pocket with a depth of 6.35 mm was then filled with a particle packet and covered with tape. The tape was necessary to secure the particle bed during loading of the test article into the test vessel due to the significant jostling present in the loading process. The test articles were placed in the containment vessel, oriented vertically so the particles were held in place by gravity before detonation as well as by the tape. A series of traverses were used to align the center of the test article with the proton beam. The tape had a small, randomly oriented slit cut in the center to prevent blowout from trapped air and to ensure the bed was under vacuum.

Figure 5 shows details of the particle packet. Three packing configurations were investigated: 60%, 40%, and 20% global volume fraction. Three layers were used for each particle packet with layers separated by paper dividers. Without the paper dividers, the steel particles would force the hollow glass microspheres (HGMs) to the surface of the packet due to the extreme difference in density. As the number of layers is increased, the reduced global volume fraction of the packet approaches a true local volume fraction. However, three was the maximum number of layers possible. As the number of layers was increased, it became increasingly difficult to accurately measure such small masses of particles. The steel particles were 410 alloy, sieved between 75 and 125 μm, and obtained from Sandvik Osprey. The steel particles were packed to approximately 56% volume fraction, and no binder was used to constrain their movement. To reduce the volume fraction, two of the configurations substituted HGMs for some portion of the steel particles. The HGMs are

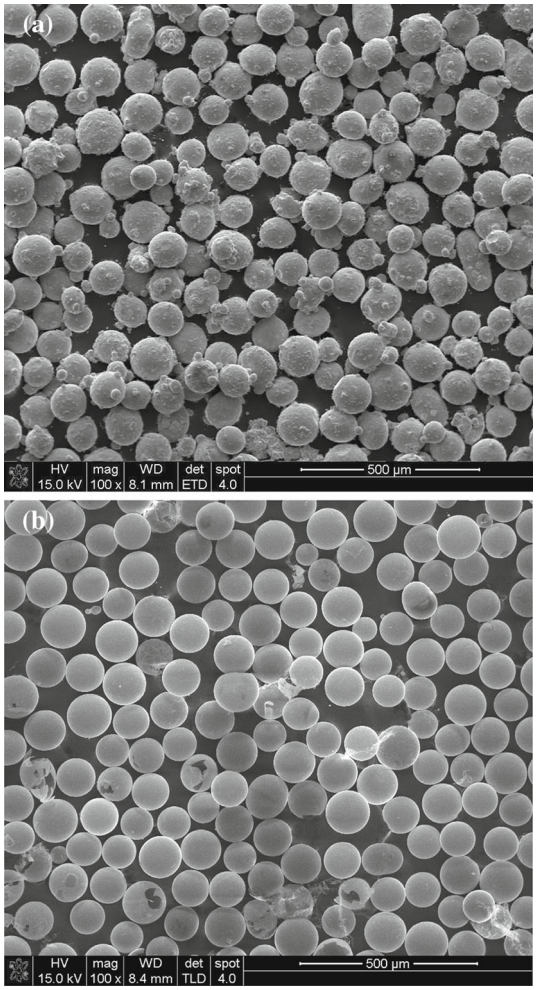

Fig. 6 SEM images of the particles at x100 magnification. **a** Steel particles sized 75–125 µm and obtained from Sandvik Osprey. **b** Hollow glass microspheres sized 90–125 µm and obtained from Cospheric

sized 90–125 µm and obtained from Cospheric. The manufacturer reports the HGMs have a bulk density of 0.09 g/cm^3. SEM images of the particles are shown in Fig. 6. The details of the five shots conducted in October 2017 (Shots 1–5) are summarized in Table 1 with the packing configuration and the resulting global volume fraction of the particle packet.

3.3 HGM failure energy

To capture a conservative estimate of the energy absorbed by crushing the HGM particles, the following steps were taken. First, the strain energy density, u, of a material may be obtained via integration of its stress–strain curve. If the integration is performed over the entirety of the curve to the breakage strain, one may obtain the failure energy, the so-called modulus of toughness, T. For a brittle material such as glass, the area under the may curve may be estimated by:

$$T = \frac{\sigma_U \epsilon_U}{2}, \tag{1}$$

where σ_U is the ultimate strength and ϵ_U is the ultimate strain. While the ultimate stress varies widely in glass, Watkins and Prado [29] show that 1 GPa is a generous failure strength for solid glass spheres. The ultimate strain has been reported by Pukh et al. [30] for a variety of glass materials to be approximately 10%. The modulus of toughness is estimated to be approximately 50 MPa. Note this is far above the manufacturer reported 2 MPa.

Second, the modulus of toughness may be considered the energy per unit volume required to crush the HGM. A representative volume must then be constructed to obtain the energy required to break the spherical shell. The average particle diameter of the HGM is 107.5 µm. SEM images similar to the one shown in Fig. 6b measure the shell thickness to be approximately 2 µm. The volume of a HGM is therefore about 35,000 µm^3. The failure energy for a representative HGM particle is then about 1.8 µJ. In both the 40% and 20% particle volume fraction tests, there are $O(10^5)$ HGM particles resulting in 0.18 J to break all the HGM particles.

Third, the energy released per unit mass is reported to be 5.5 MJ/kg by Johnson [31] for PBX-9501. The pellet used has a mass of 2.8 g and gives an energy release of approxi-

Table 1 Shot table for the proton radiography tests showing the shot number, packing configuration (see Fig. 5), global volume fraction, and ambient conditions

Shot	Packing config.	ϕ	Ambient	Temp. (K)	Press. (kPa)
1	1	0.575	Vacuum	–	–
2	1	0.571	Vacuum	–	–
3	2	0.384	Vacuum	–	–
4	3	0.196	Vacuum	–	–
5	3	0.197	Vacuum	–	–
6	1	0.561	Air	298.6	101.67
7	1	0.560	Xenon	297.3	100.13
8	1	0.566	SF_6	298.5	100.22
9	1	0.567	Air	299.2	100.32
10	1	0.561	Vacuum	–	–

mately 15.4 kJ. The ratio of HGM failure energy to released explosive energy is less 0.01%.

3.4 Varying carrier fluid tests

A set of experiments varying the carrier fluid, designated Shots 6–10, were conducted in November 2018 and are summarized in Table 1. The test article used was the same as that detailed in Fig. 3a. The packing configuration was kept constant in this series of tests (all tests used the first packing configuration to maintain a 60% global volume fraction). Instead, the test article was wrapped with a 3.18-mm-thick aluminum cylinder to contain the various carrier phases. The gas cylinder extended to a height of 23 cm above the test article with an inner diameter of 12.7 cm. A gas handling system was used to ensure each cylinder was brought to 100 ± 2 kPa pressure and the temperature recorded to determine the initial thermodynamic state of the gas. Xenon and SF_6 were chosen for their large nuclear cross sections in an unsuccessful attempt to capture the shock with the proton radiography. A series of traverses were used to align the center of the test article with the proton beam.

The test article was attached to the aluminum casing with a aluminum restraining ring, shown in Fig. 7a. The screws used to attach the restraining ring were used as alignment fiducials. The step wedge consisted of 10 evenly spaced steps along its 30.25 mm length, each with a 1.03-mm change in thickness. The step wedge was used to normalize the radiographs in the case of fluctuating proton beam energy. A single photon Doppler velocimetry (PDV) probe with 40 mm working distance and 0.43 mm light diameter was suspended above the particle bed on a stand. However, the PDV probe results were not conclusive and are excluded from this investigation for brevity. The assembled aluminum gas container is shown on the test stand in Fig. 7b.

4 Input uncertainty quantification

4.1 Uncertainty of the explosive length, diameter, and density

Each PBX-9501 pellet was characterized by measurement of its diameter and length with calipers (±0.05 mm measurement uncertainty). The pellets were inspected to ensure they were free of chips or scratches, and the mass of the pellets was measured with a mass balance (±0.0001 g measurement uncertainty). Assuming a perfect cylinder, the volume of the explosive is calculated and the density derived. The explosive density is compared to the theoretical maximum density of 1.855 [32]. Results are summarized in Table 2. Note the diameter, length, and density of the explosive demonstrate less than 0.8% variability.

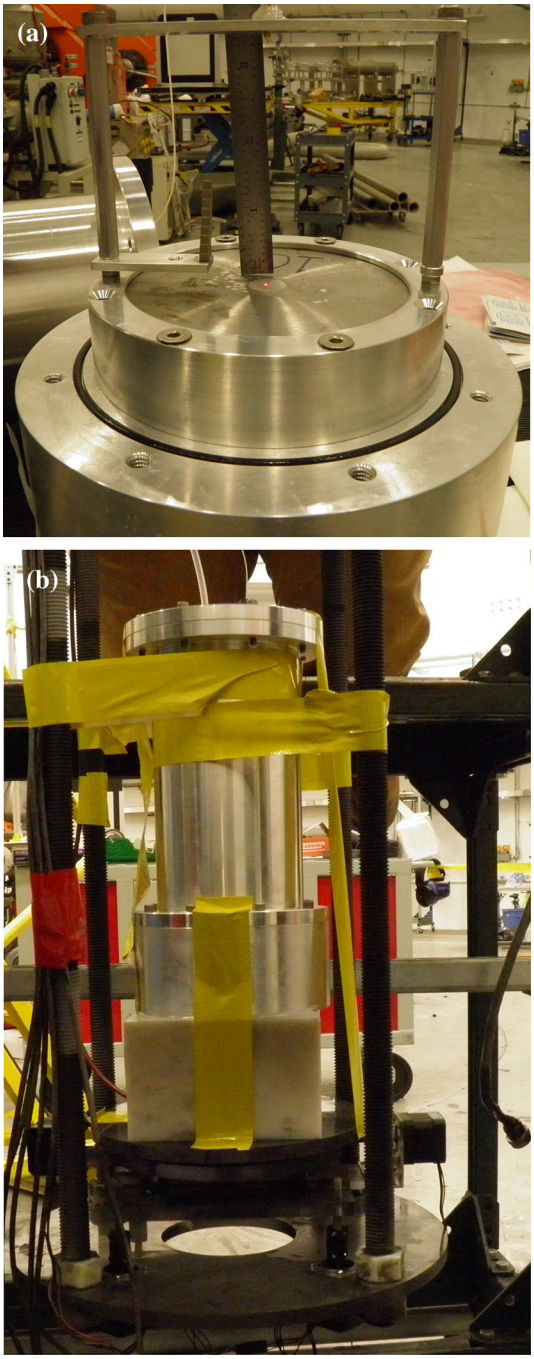

Fig. 7 Details of the November 2018 test setup used for Shots 6–10. **a** Test article with aluminum retaining ring, step-wedge fiducial, and PDV probe. **b** Assembled aluminum casing with test article mounted on the test stand

4.2 Uncertainty of the explosive casing

Dimensions of the explosive casing considered critical for simulation were measured with calipers (±0.05 mm measurement uncertainty). Results are summarized in Table 3. The bore refers to the top portion of the hole through the

Table 2 Measured length, diameter, and density of the PBX-9501 pellets with comparison to the percent theoretical maximum density (% TMD)

Shot	Dia. (mm)	Length (mm)	Mass (g)	Dens. (g/cm^3)	TMD (%)
1	12.71	12.74	2.849	1.76	95.0
2	12.73	12.69	2.847	1.76	95.1
3	12.73	12.70	2.848	1.76	95.0
4	12.73	12.73	2.847	1.76	94.8
5	12.73	12.73	2.847	1.76	94.8
6	12.70	12.78	2.839	1.75	94.6
7	12.78	12.67	2.839	1.75	94.2
8	12.83	12.70	2.839	1.73	93.3
9	12.75	12.80	2.838	1.74	93.6
10	12.75	12.83	2.839	1.73	93.4
μ	12.74	12.74	2.843	1.75	94.4
σ	0.04	0.05	0.005	0.01	0.7

The value used for TMD is 1.855

Table 3 Measured dimensions of the explosive casing

Shot	Bore		Total	Outer
	Dia.	Depth	thickness	dia.
1	13.11	19.07	38.01	102.52
2	13.12	19.08	38.02	102.50
3	13.15	19.09	38.05	102.52
4	13.15	19.12	38.07	102.55
5	13.15	19.11	38.05	102.50
6	13.10	19.11	38.08	102.48
7	13.12	19.08	38.04	102.62
8	13.18	19.06	38.11	102.48
9	13.16	19.08	38.13	102.57
10	13.20	19.11	38.10	102.61
μ	13.14	19.09	38.06	102.54
σ	0.03	0.02	0.05	0.05

Note the casing dimensions exhibit less than 0.3% variability. Measurements are in millimeters

Table 4 Mass of steel (St) and hollow glass microspheres (HGMs) particles in each layer in grams

Shot	Layer 1		Layer 2		Layer 3	
	St	HGM	St	HGM	St	HGM
1	1.2300	–	1.2297	–	1.2296	–
2	1.2303	–	1.2294	–	1.2295	–
3	0.8202	0.0051	0.8197	0.0050	0.8203	0.0048
4	0.4104	0.0098	0.4102	0.0096	0.4097	0.0103
5	0.4094	0.0098	0.4103	0.0096	0.4096	0.0099
6	1.2330	–	1.2326	–	1.2328	–
7	1.2332	–	1.2317	–	1.2329	–
8	1.2322	–	1.2305	–	1.2335	–
9	1.2344	–	1.2310	–	1.2325	–
10	1.2297	–	1.2326	–	1.2323	–

The error of the masses with respect to the nominal was less than 0.4% for the steel particles and less than 5% for the HGM

center of the cylindrical casing where the explosive pellet and particle packet are located, as shown in Fig. 3a. The depth is from the top of the casing to the small step on which the explosive rests. Total thickness refers to the length of the cylindrical casing, while outer diameter refers to the diameter of the casing. Note the casing dimensions exhibit less than 0.3% variability.

4.3 Particle packet uncertainty

Particle packets were constructed by careful measurement of the particle layer mass on a mass balance (measurement uncertainty of ± 0.0001 g). After measuring their mass, particles were then poured into the awaiting pocket formed by the casing and the explosive and settled with a minimum of shaking and vibration. Layers were separated by paper dividers, diameter of 13.0 ± 0.1 mm and thickness of $89 \pm 3\,\mu$m, and topped with a piece of tape. Results are summarized in Table 4. Examination of the configuration 1 shots (1, 2, and 6–10) provide a measure of the variability present in the packing process. Each steel particle layer was 1.232 ± 0.001 g, and the total mass was 3.695 ± 0.004 g. Referring to Fig. 5 for nominal masses for each layer, the error of the masses with respect to the nominal was less than 0.4% for the steel particles and less than 5% for the HGM. The extremely small masses of the HGM prevented their accurate weighing, especially for Shot 3.

Results for the global volume fraction are shown in Table 5. The global volume fraction of the particle bed is calculated as the ratio of the bulk density to the steel particle density, 7.655 ± 0.009 g/cm^3, measured in Hughes et al. [33]. The contribution of the HGM is neglected due to the much greater density of the steel particles. The bulk density of the

Table 5 Volume fraction of the particle packet

Shot	Total mass (g)	Depth (mm)	Bulk dens. (g/cm^3)	ϕ
1	3.689	6.38	4.40	0.575
2	3.689	6.38	4.37	0.571
3	2.475	6.38	2.94	0.384
4	1.260	6.35	1.50	0.196
5	1.259	6.34	1.50	0.197
6	3.698	6.55	4.30	0.561
7	3.698	6.55	4.29	0.560
8	3.696	6.43	4.33	0.566
9	3.698	6.43	4.34	0.567
10	3.695	6.45	4.29	0.561

The nominally repeated shots observed an approximately 1% variability

particle bed is obtained as the ratio of the particle mass to the bed volume. The total mass of the particles is obtained from summation of the masses listed in Table 4. The depth of the particle bed was measured as the distance from the top of the casing to the top of epoxied explosive. The depth after bonding exhibits less than 1.3% uncertainty. The reader will note that a small annular region exists between the explosive and the casing. Some particles were observed to fill into this gap during the loading process. However, the gap is small enough that its inclusion in the volume fraction calculation lowers the global volume fraction only 0.001. The results presented include this annular region and subtract the small volume of the paper dividers. Examining the nominally repeated shots (1, 2, and 6–10), the bed global volume fraction was observed to be 0.566 ± 0.006, which is an approximately 1% variability.

4.4 Summary of uncertainties

A summary of the uncertainties associated with experiments is included in Table 6. Further details for each input may be obtained from the respective section. Results for each value are presented as $\mu \pm 1\sigma$ and are listed with the method used to obtain each value. Significant work has been done to quantify the particle density, size distribution, and local volume fraction in a previous investigation [33].

Table 6 Summary table of the uncertain inputs quantified for the tests

Parameter	Value	Method
Explosive diameter	12.74 ± 0.04 mm	Calipers
Explosive length	12.74 ± 0.05 mm	Calipers
Explosive density	1.75 ± 0.01 g/cm^3	Derived quantity
Bore diameter	13.14 ± 0.03 mm	Calipers
Bore depth	19.09 ± 0.02 mm	Calipers
Layer mass*	1.232 ± 0.001 g	Mass balance
Total mass*	3.695 ± 0.004 g	Mass balance
Particle bed depth	6.42 ± 0.08 mm	Calipers
Particle diameter	$115 \pm 23\,\mu$m	SEM analysis
Particle density	7.655 ± 0.009 g/cm^3	Gas pycnometer
Local vol. fract.	0.545 ± 0.004	CT scan
Global vol. fract.*	0.566 ± 0.006	Derived quantity

Uncertain inputs marked with an asterisk are values obtained from the nominally repeated shots (1, 2, and 6–10)

5 Results

5.1 Transmission radiographs

The time evolution of the six different test conditions is shown in Fig. 8. First, with regard to the varying volume fraction tests conducted in vacuum, the 60% volume fraction configuration (Fig. 8a) displayed a piston-like behavior as it was expelled by the explosive. The three initial layers, formed by the paper dividers, maintained their structure as they traveled downstream and exhibited minimal spreading. At late times, some fracturing of the layers was exhibited, similar to the bed fracturing postulated by Frost [34] to be responsible for the instabilities observed at the large scale. The 40% volume fraction configuration (Fig. 8b) has the three-layer structure initially visible as it exits the casing but quickly devolves into a cloud as it travels downstream. The 20% volume fraction configuration exited as a cloud with single denser line present and shows the most stochastic nature of all the tests. The overall shape was observed to be largely different in curvature between the repeated tests for the 20% case (not shown). The repeated test of the 20% volume fraction configuration showed the ends of the particle bed racing ahead of the center portion, similar to that shown in Fig. 8a. In contrast, the repeated test of the 60% volume fraction configuration showed consistent behavior.

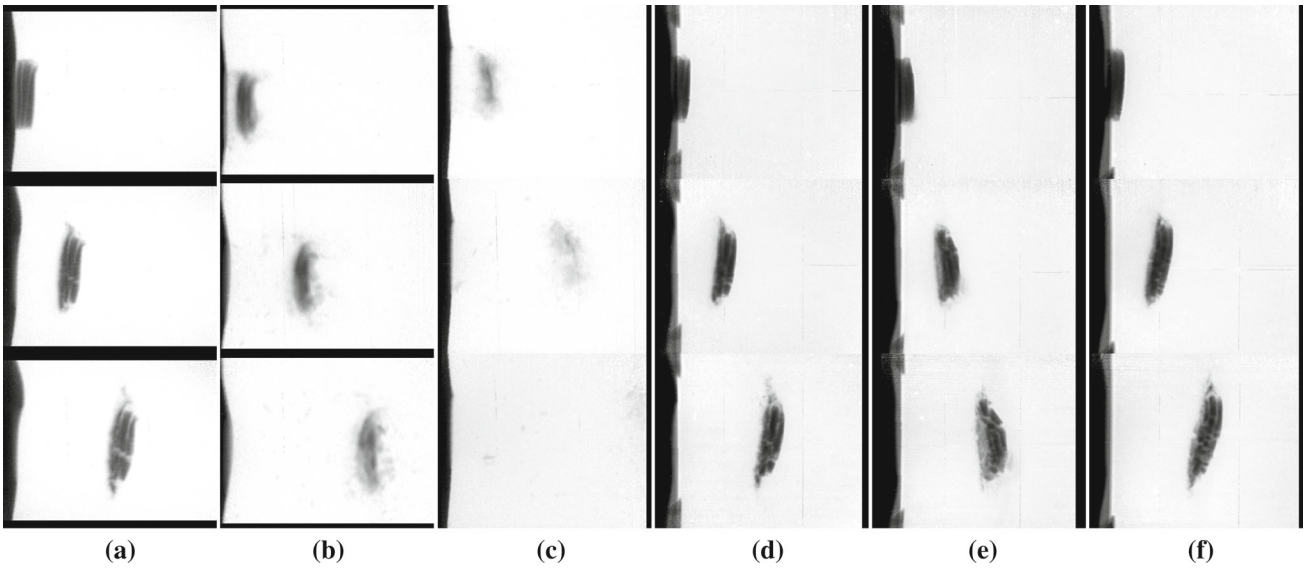

Fig. 8 Transmission radiographs for 13.8 μs (top), 23.8 μs (middle), and 34.8 μs (bottom) after detonation. Flow is from left to right. **a** The 60% volume fraction configuration displayed a piston-like behavior as it was expelled by the explosive. **b** The 40% volume fraction configuration had a three-layer structure initially visible as it exited the casing but quickly devolves into a dispersed cloud. **c** The 20% volume fraction configuration exited as a cloud with single denser line present and shows the most stochastic nature (the particles have exited the frame by the final time stamp). The three different ambient conditions investigated (**d** air, **e** xenon, and **f** SF_6) show very similar behavior when dispersed, with some structural differences present at late time

The HGMs are clearly crushed during the early time. As particles move through the weak layer of glass particles, they build momentum and collide with subsequent layers. The resulting collisions destroy the order of the layers and spread the steel particles in a stochastic manner. Coupled with the decreased mass present in the particle bed, the relative motion quickly disperses the particle bed. The close packing of the 60% volume fraction prevents the particles from gaining momentum with respect to one another and only displays fractures and some slow deformation at late time.

Next, with regard to the 60% volume fraction configuration with varying ambient fluids, the piston-like behavior is maintained as it is expelled by the explosive with the characteristic observed. Though small differences in structure and spreading are apparent, the particles are remarkably close to each other considering the varying initial conditions (Fig. 8d–f). Note that an aluminum ring was placed around the lip of the steel casing to secure it and is visible in the radiographs as a thin layer of less dense material above the dark steel casing. Two screws used to secure the restraining ring are also visible at the edges of the radiographs.

5.2 Front detection

Particle fronts were determined from thresholding of the transmission intensity. First, images were rotated to align the casing with the image axes. Next, a moving average was applied to the image intensity with a 17-pixel window size to prevent spurious front detection. Third, a background threshold was determined for each image line by an average of 100 pixels in an undisturbed portion of the image, such as the right hand side of the image. Fourth, the initial casing location was determined as the location in the first image where the intensity drops below 23% of the background threshold. The 23% casing location threshold was determined by iteration to match the thickness of the 2.60 ± 0.05-mm aluminum retaining ring present in the November 2018 radiographs. By using this threshold value, the thickness of the ring was measured to be 2.6 ± 0.1 mm. Finally, the downstream front was determined as the image location where the intensity drops below 90% of the background and the upstream front is where the intensity rises again above the 90% threshold. Greater threshold values, such as 95% and 98%, were attempted but produced too many spurious front locations.

Figure 9a shows an example line profile with the upstream and downstream particle fronts identified. Note the relatively sharp drop in image intensity at the particle front. Particle fronts overlaid on the original radiograph are shown in Fig. 9b. However, while no spurious detections are shown in Fig. 9b, spurious detections did occur. For instance, the seam down the center of the image is a scintillator tile artifact and is of sufficient contrast that it sometimes trips the particle front algorithm.

These outliers were removed with a three-step process. First, the outlier detection algorithm of Goring and Nikora

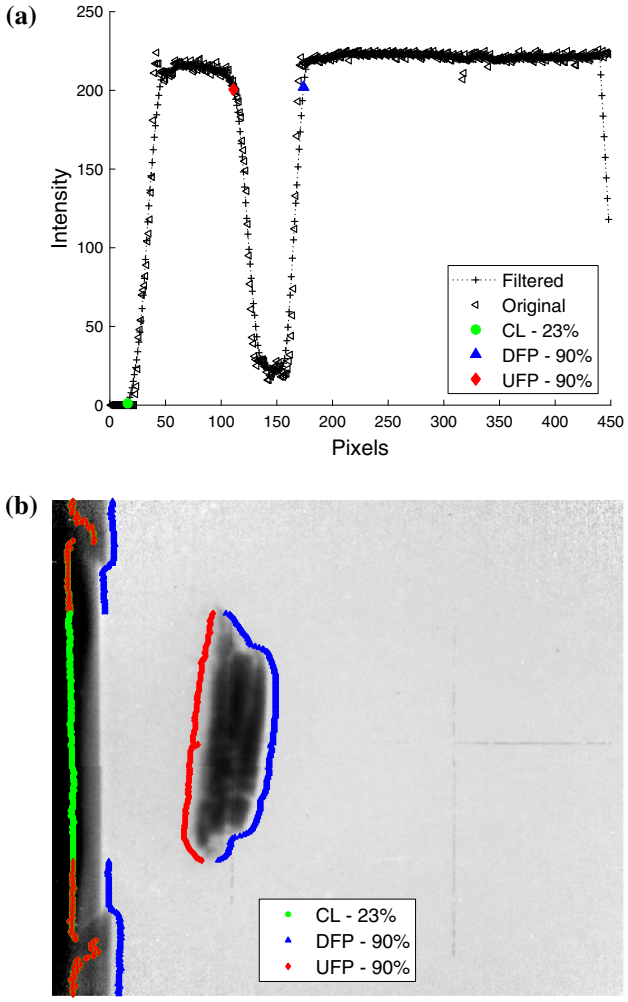

Fig. 9 Processing technique used to extract particle fronts from the radiographs. **a** Sample line profile showing the selection of the downstream front position (DFP), upstream front position (UFP), and casing location (CL) at the centerline, 23.8 μs after detonation. Note the CL is obtained from the first image and is overlaid here on the line profile for reference. **b** Front tracking results overlaid on the Shot 1 radiograph 23.8 μs after detonation

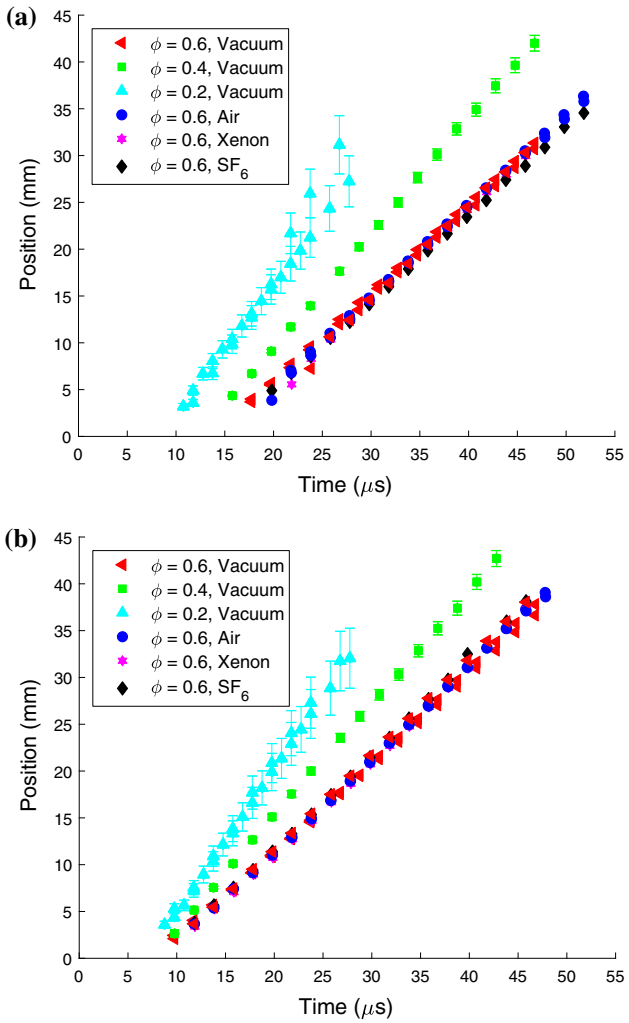

Fig. 10 Particle front position at the centerline of the particle packet for **a** upstream front position and **b** downstream front position

[35], with correction by Wahl [36], was applied to the particle front positions. The outliers were replaced by cubic interpolation using 12 points on either side of the detected outlier. The MATLAB code used was provided by Mori et al. [37]. Second, a mask was constructed to eliminate the casing detections. The mask was chosen just past the casing, retaining rings, and screws. Third, the mask was applied to the despiked particle front positions.

The front positions of the particle packets at the centerline were extracted and are plotted in Fig. 10. The initial time is from the detonator initiation. Images are not collected until after an approximately $5.78 \pm 0.04\,\mu s$ interval to account for the delay of the detonator to activate and for the explosive to completely react. The current viewing resistor used to determine the initial time has an uncertainty of $\pm 0.04\,\mu s$.

To attempt to capture the uncertainty present in the particle front determination, the threshold was perturbed by ±5%. The resulting change in the particle front is captured in the error bars of the front position. The 60% volume fraction configuration (including the varying ambient fluid cases) shows an approximately 1% variation. The lower volume fractions of 40% and 20% show a 2% and 10% variation, respectively, due to the greater spread of particles that decreases the steepness of the intensity curve.

The experimental conditions with repeated tests show close agreement on the centerline except for the upstream front position of the 20% volume fraction. The 20% upstream volume fraction was quite dilute at late times, and the front began to be lost against the background noise. One may observe an increase in overall packet velocity as the total mass of the particle bed is decreased with the addition of HGM. The particle packet therefore behaves as though it were a single object of decreased density being acted on by a force of con-

stant magnitude. The 20% volume fraction quickly exited the field of view for the 2 μs inter-frame time and so relatively few data points were recovered in Shot 4. The inter-frame timing was decreased in Shot 5 to prevent this issue. Note that the fronts move in a largely linear fashion, indicating that the particles receive their momentum impulsively in the passage of the contact discontinuity. Furthermore, comparing the results of the four gas shots with the vacuum shot, we note that the results are within close agreement. The vacuum shot lacks an ambient medium for a shock to form, suggesting that the contact interface between the ambient and the detonation products is almost solely responsible for the delivered impulse.

5.3 Comparison to Gurney velocity

The Gurney model [38] was derived to estimate the peak velocity imparted to a metal layer propelled by an explosive. Gurney assumed that that the explosive energy was instantaneously converted into kinetic energy, partitioned between the explosive products and the dispersed metal. Additionally, it is assumed that the explosive products are of uniform density and that their radial velocity varies linearly from the origin to the metal–explosive interface. The piston-like motion of the 60% volume fraction cases invites a comparison between dispersed particle beds and Gurney's model. The main difference between the Gurney model and the experiments presented here, however, is the pre-fragmented nature of the bed, whereas Gurney derives the velocity of the metal layer before it undergoes fragmentation.

Milne [39] has recently worked to extend the Gurney equations to a porous bed by fitting to the results of simulations, providing fits for both spherical and cylindrical geometries. While some experimental validation is presented in Milne's work, Loiseau et al. [40] provided extensive experimental validation for granular beds, both dry and wetted. Interestingly, Loiseau et al. showed that the wetted granular beds scaled with the classical Gurney relations, while the dry beds followed the porous Gurney relations developed in Milne. Milne showed that the loss of velocity between solid shells and porous beds is due to the collapse of the pores within the particle bed, resulting in additional PdV heating of the bed. Loiseau et al. further postulated that the liquid within the wetted bed prevents this pore collapse, which is why no loss of velocity is shown in the wetted beds.

The downstream front position is sufficiently linear that a first-order polynomial, with a minimum R^2 of 0.99, may be fit to the position data to extract a single front velocity. Different expressions of Gurney velocity have been advanced depending on the shape and nature of the explosively propelled object. While none of these relations is an exact match for the experimental setup, several relations may be used to bound the possible Gurney velocities. Forming the upper bound, the Gurney velocity, V_{IT}, for an infinitely tamped sandwich is:

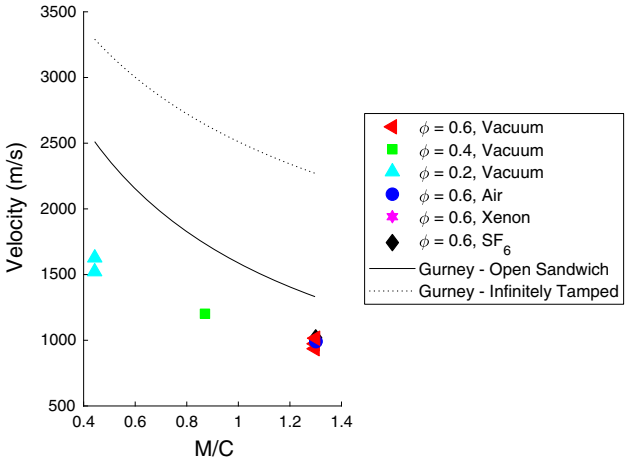

Fig. 11 Comparison of particle front velocity with equivalent Gurney velocities

$$\frac{V_{\mathrm{IT}}}{\sqrt{2E}} = \left(\frac{M}{C} + \frac{1}{3}\right)^{(-1/2)}, \tag{2}$$

where C is the mass of the explosive (approximately 2.8 g) and M is the mass of the particle packet (see Table 4). The Gurney constant, $\sqrt{2E}$, for PBX-9501 is taken from the literature as 2.90 km/s [41]. Forming the lower bound, the Gurney velocity, V_{OS}, for an open sandwich is:

$$\frac{V_{\mathrm{OS}}}{\sqrt{2E}} = \left(\frac{1 + \left(1 + 2\frac{M}{C}\right)^3}{6\left(1 + \frac{M}{C}\right)} + \frac{M}{C}\right)^{-1/2}. \tag{3}$$

Other Gurney relations, such as the spherical configuration and the porous Gurney relations of Milne [39], lie in between these two relations. The particle front velocities are plotted with their equivalent Gurney velocities in Fig. 11. It is apparent that the particle front velocities are appreciably lower. At the 60% volume fraction, the M/C is 1.3 and the relative difference between the averaged front velocity between all cases and the open sandwich Gurney velocity is approximately 23%. At 20% volume fraction, the relative difference increases to 38%. Qualitatively, the reduction of the porous bed velocity below that of predicted Gurney velocity is consistent with results of Loiseau et al. [40]. Unfortunately, no work similar to Milne's [39] but with the open sandwich geometry yet exists within the literature to provide a more quantitative comparison. These results also provide a basic check on the data, showing the particle front velocity does indeed begin to approach the Gurney velocity as the volume fraction approaches the 100% volume fraction assumption of the Gurney relations. It also underscores the loss of energy coupling due largely to the compaction of the bed and pore

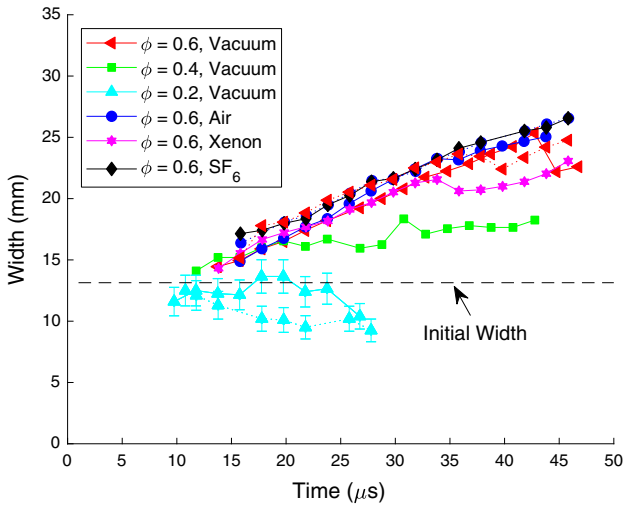

Fig. 12 Width of the particle packet extracted at each frame. The initial width is marked with a dashed black line. The width from Shot 1 is not presented as the entire front is not captured within the frame. Data from individual shots are connected with lines for the convenience of the reader

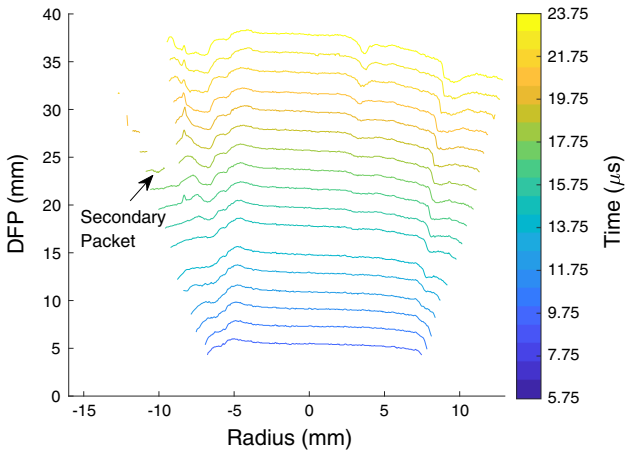

Fig. 13 The downstream particle front time evolution of Shot 2 shows an example of the pinch-off phenomenon. A secondary packet particle becomes isolated from the main packet at 34.75 μs and then disappears against the background at 44.75 μs, leading to a sharp decrease in the measured width

collapse [39], but also to other processes such as flow being channeled through the narrow spaces between particles, collisions, etc. Note the mass of the detonator, approximately 0.6 g of explosive, may be included in the analysis resulting in a decrease in the M/C values observed but with no difference in the conclusions.

5.4 Packet width

The width of the particle packet, extracted from the particle fronts, is plotted in Fig. 12 and compared to the initial width. The 60% volume fraction cases show an increasing width with time. Note the vacuum, xenon, air, and SF_6 do not show an appreciable difference in spreading, reinforcing the conclusions from the centerline front positions. Interestingly, some of the cases show a "pinch-off"-type phenomenon where portions at the edge of the bed separate and then disperse from the main particle packet. This behavior can be demonstrated in Fig. 13. The downstream particle front is plotted as a function of time. A hole develops in the front where a portion of the bed peels off and then quickly disperses such that it is lost by the tracking algorithm. In Fig. 12, this phenomenon manifests itself as a drop in width when the secondary particle packet is no longer detected by the algorithm.

The 40% volume fraction shows growth at early time and then approaches an asymptotic width of approximately 18 mm. The 20% volume fraction cases show two different behaviors. In one case, the width slightly increases over the initial width and then decreases. In the other case, the width decreases and then levels off. In both cases, around 25 μs the low amount of particles begins to disappear against the background and the width quickly decreases, followed by the packet exiting the frame.

6 Conclusions

The series of experiments presented in this paper provide new validation data for the regime of moderate-to-high volume fraction and high-Mach-number flow. In addition, the current set of experiments improves upon a previous set of unpublished experiments performed at Eglin AFB. The previous set of experiments did not sufficiently quantify the initial volume fraction, and the multiple exposure X-ray diagnostic did not allow for rigorous determination of the particle front, degrading their usefulness for validation efforts.

Ten explosive tests were performed at the Los Alamos Neutron Science Center Proton Radiography facility. A 13 × 6 mm cylindrical packet of 115-μm steel particles was dispersed by 2.8 g of PBX-9501. The protons pierce the opaque explosive products produced during detonation to provide 21 to 24 time-resolved images of the particle fronts with a 45-mm-by-45-mm field of view and a resolution of 50 μm/pixel. As the data are intended for validation, a summary of the uncertain inputs for the experiments is included in Table 6.

The first five tests, performed in October 2017, investigated three packing configurations: 60%, 40%, and 20% global volume fraction. Three layers were used for each particle packet with layers separated by paper dividers. To reduce the global volume fraction, two of the configurations substituted HGMs for some portions of the steel particles. Transmission radiographs show very different behaviors for

the three configurations. The 60% volume configuration shows a piston-like behavior as it is expelled by the explosive. The 40% volume fraction configuration has the three-layer structure initially visible as it exits the casing but quickly devolves into a cloud as it travels downstream. The 20% volume fraction case exits as a cloud with single denser line present and shows a greater stochastic nature. Lower volume fractions were accelerated to higher velocities, behaving as though they were a single object of decreased density being acted on by a force of constant magnitude.

The second set of five tests, performed in November 2018, examined the dispersal of the particle packet into three different carrier fluids: air, xenon, and SF_6. The transmission radiographs of the three different carrier fluids and the 60% vacuum shots show very similar behavior with only minimal differences in spreading that are not necessarily attributable to the different carrier fluids.

The centerline particle fronts for the three carrier phases demonstrate close agreement, suggesting the ambient carrier phase has little impact on the dispersal of the particles in this regime. The forces exerted on the particle bed by the dense, propagating explosive products are dominant. Furthermore, the results demonstrate a highly linear behavior during this early time suggesting that the particles are impulsively acted upon by the contact interface and the shock. Finally, comparing the results of the four gas shots with the three vacuum shots, we note that the results are within close agreement. The vacuum shot lacks an ambient medium for a shock to form, suggesting that the contact interface is almost solely responsible for the delivered impulse. Comparison of the particle front velocity with the peak velocity predicted by the Gurney model shows the particles are dispersed significantly slower, demonstrating the significant loss of energy coupling due to flow channeling through the particle bed, compaction, etc.

However, as this study only presents the motion of the particle cloud, additional tests are needed to validate the accompanying particle–fluid interaction and explosive model. Tests of similar configuration, but that offer information on the behavior of the gas, such as the shock and contact interface at early time, are needed to provide these necessary prediction metrics.

Acknowledgements The authors would like to acknowledge the efforts of the Proton Radiography experimental personnel at Los Alamos National Laboratory for their hard work in conducting the experiments. The authors would like to thank Matthew Freeman for offering his expertise on imaging with proton radiography. This work was supported by the U.S. Department of Energy, National Nuclear Security Administration, Advanced Simulation and Computing Program, as a Cooperative Agreement under the Predictive Science Academic Alliance Program, under Contract No. DE-NA0002378.

References

1. Zhang, F., Frost, D., Thibault, P., Murray, S.: Explosive dispersal of solid particles. Shock Waves **10**(6), 431–443 (2001). https://doi.org/10.1007/PL00004050
2. Frost, D.L., Zarei, Z., Zhang, F.: Instability of combustion products interface from detonation of heterogeneous explosives. 20th International International Colloquium on the Dynamics of Explosion and Reactive Systems, Montreal, Canada, pp. 1–6 (2005)
3. Frost, D.L., Ornthanalai, C., Zarei, Z., Tanguay, V., Zhang, F.: Particle momentum effects from the detonation of heterogeneous explosives. J. Appl. Phys. **101**(11), 113529 (2007). https://doi.org/10.1063/1.2743912
4. Frost, D.L., Grégoire, Y., Petel, O., Goroshin, S., Zhang, F.: Particle jet formation during explosive dispersal of solid particles. Phys. Fluids **24**(9), 091109 (2012). https://doi.org/10.1063/1.4751876
5. Sun, M., Saito, T., Takayama, K., Tanno, H.: Unsteady drag on a sphere by shock wave loading. Shock Waves **14**(1–2), 3–9 (2005). https://doi.org/10.1007/s00193-004-0235-4
6. Tanno, H., Itoh, K., Saito, T., Abe, A., Takayama, K.: Interaction of a shock with a sphere suspended in a vertical shock tube. Shock Waves **13**(3), 191–200 (2003). https://doi.org/10.1007/s00193-003-0209-y
7. Tanno, H., Komuro, T., Takahashi, M., Takayama, K., Ojima, H., Onaya, S.: Unsteady force measurement technique in shock tubes. Rev. Sci. Instrum. **75**(2), 532–536 (2004). https://doi.org/10.1063/1.1641156
8. Bredin, M., Skews, B.: Drag measurement in unsteady compressible flow. Part 1: An unsteady flow facility and stress wave drag Balance, R&D. J. S. Afr. Inst. Mech. Eng. **23**(1), 3–12 (2007)
9. Maxey, M.R., Riley, J.J.: Equation of motion for a small rigid sphere in a nonuniform flow. Phys. Fluids **26**(4), 883–889 (1983). https://doi.org/10.1063/1.864230
10. Gatignol, R.: The Faxén formulas for a rigid particle in an unsteady non-uniform Stokes-flow. J. Mec. Theor. Appl. **2**(2), 143 (1983)
11. Parmar, M., Haselbacher, A., Balachandar, S.: Generalized Basset-Boussinesq-Oseen equation for unsteady forces on a sphere in a compressible flow. Phys. Rev. Lett. **106**(8), 084501 (2011). https://doi.org/10.1103/PhysRevLett.106.084501
12. Parmar, M., Haselbacher, A., Balachandar, S.: Equation of motion for a sphere in non-uniform compressible flows. J. Fluid Mech. **699**(5), 352–375 (2012). https://doi.org/10.1017/jfm.2012.109
13. Annamalai, S., Balachandar, S.: Faxén form of time-domain force on a sphere in unsteady spatially varying viscous compressible flows. J. Fluid Mech. **816**, 381–411 (2017). https://doi.org/10.1017/jfm.2017.77
14. Black, W.J., Denissen, N., McFarland, J.A.: Particle force model effects in a shock-driven multiphase instability. Shock Waves **28**(3), 463–472 (2018). https://doi.org/10.1007/s00193-017-0790-0
15. Britan, A., Elperin, T., Igra, O., Jiang, J.: Acceleration of a sphere behind planar shock waves. Exp. Fluids **20**(2), 84–90 (1995). https://doi.org/10.1007/BF00189297
16. Jourdan, G., Houas, L., Igra, O., Estivalezes, J.L., Devals, C., Meshkov, E.: Drag coefficient of a sphere in a non-stationary flow: new results. Proc. R. Soc. A Math. Phys. Eng. Sci **463**(2088), 3323–3345 (2007). https://doi.org/10.1098/rspa.2007.0058
17. Wagner, J.L., Beresh, S.J., Kearney, S.P., Pruett, B.O.M., Wright, E.K.: Shock tube investigation of quasi-steady drag in shock-particle interactions. Phys. Fluids **24**(12), 123301 (2012). https://doi.org/10.1063/1.4768816

18. Bordoloi, A.D., Martinez, A.A., Prestridge, K.: Relaxation drag history of shock accelerated microparticles. J. Fluid Mech. **823**, R4 (2017). https://doi.org/10.1017/jfm.2017.389
19. Hughes, K., Balachandar, S., Kim, N.H., Park, C., Haftka, R., Diggs, A., Littrell, D.M., Darr, J.: Forensic uncertainty quantification for experiments on the explosively driven motion of particles. J. Verif. Valid. Uncertain. Quantif. **3**(4), 041004 (2019). https://doi.org/10.1115/1.4043478
20. Rudinger, G.: Some properties of shock relaxation in gas flows carrying small particles. Phys. Fluids **658**(1964), 658–663 (1964). https://doi.org/10.1063/1.1711265
21. Wagner, J.L., Beresh, S.J., Kearney, S.P., Trott, W.M., Castaneda, J.N., Pruett, B.O., Baer, M.R.: A multiphase shock tube for shock wave interactions with dense particle fields. Exp. Fluids **52**(6), 1507–1517 (2012). https://doi.org/10.1007/s00348-012-1272-x
22. Kellenberger, M., Johansen, C., Ciccarelli, G., Zhang, F.: Dense particle cloud dispersion by a shock wave. Shock Waves **23**(5), 415–430 (2013). https://doi.org/10.1007/s00193-013-0432-0
23. Dullien, F.: Porous Media: Fluid Transport and Pore Structure, 2nd edn. Elsevier Science, San Diego (1992). https://doi.org/10.1016/C2009-0-26184-8
24. Rodriguez, V., Saurel, R., Jourdan, G., Houas, L.: Impulsive dispersion of a granular layer by a weak blast wave. Shock Waves **27**(2), 187–198 (2017). https://doi.org/10.1007/s00193-016-0658-8
25. King, N., Ables, E., Adams, K., Alrick, K., Amann, J., Balzar, S., Barnes Jr., P., Crow, M., Cushing, S., Eddleman, J., Fife, T., Flores, P., Fujino, D., Gallegos, R., Gray, N., Hartouni, E., Hogan, G., Holmes, V., Jaramillo, S., Knudsson, J., London, R., Lopez, R., McDonald, T., McClelland, J., Merrill, F., Morley, K., Morris, C., Naivar, F., Parker, E., Park, H., Pazuchanics, P., Pillai, C., Riedel, C., Sarracino, J., Shelley Jr., F., Stacy, H., Takala, B., Thompson, R., Tucker, H., Yates, G., Ziock, H.J., Zumbro, J.: An 800-MeV proton radiography facility for dynamic experiments. Nucl. Instrum. Methods Phys. Res. Sect. A Accel. Spectrom. Detect. Assoc. Equip **424**(1), 84–91 (1999). https://doi.org/10.1016/S0168-9002(98)01241-8
26. Mottershead, C., Zumbro, J.: Magnetic optics for proton radiography. Proceedings of 1997 Particle Accelerator Conference (Cat. No.97CH36167), vol. 2, pp. 1397–1399. IEEE (1998). https://doi.org/10.1109/PAC.1997.750705
27. Merrill, F.E., Campos, E., Espinoza, C., Hogan, G., Hollander, B., Lopez, J., Mariam, F.G., Morley, D., Morris, C.L., Murray, M., Saunders, A., Schwartz, C., Thompson, T.N.: Magnifying lens for 800 MeV proton radiography. Rev. Sci. Instrum. **82**(10), 1037091 (2011). https://doi.org/10.1063/1.3652974
28. Mottershead, T., Barlow, D., Blind, B., Hogan, G., Jason, A., Merrill, F., Morley, K., Morris, C., Saunders, A., Valdiviez, R.: Design and operation of a proton microscope for radiography at 800 MeV. Proceedings of 2003 Particle Accelerator Conference, pp. 702–704. IEEE, Portland, OR, USA (2003) https://doi.org/10.1109/PAC.2003.1289014
29. Watkins, I.G., Prado, M.: Mechanical properties of glass microspheres. Procedia Mater. Sci. **8**, 1057–1065 (2015). https://doi.org/10.1016/j.mspro.2015.04.168
30. Pukh, V.P.: Atomic structure and strength of inorganic glasses. Phys. Solid State **47**(5), 876–881 (2005). https://doi.org/10.1134/1.1924848
31. Johnson, J.B., Wainwright, F.: Determining the equivalent explosive effect for different explosives. Proceedings of 1994 International Snow Science Workshop, pp. 31–39. Snowbird, Utah (1994)
32. Dobratz, B., Crawford, P.: LLNL explosives handbook-properties of chemical explosives and explosive stimulants, LLNL explosives handbook-properties of chemical explosives and explosive stimulants. Technical report, Lawrence Livermore National Laboratory, Livermore, CA (1985)
33. Hughes, K.T., Balachandar, S., Diggs, A., Haftka, R., Kim, N.H., Littrell, D.: Simulation-driven design of experiments examining the large-scale, explosive dispersal of particles. Shock Waves **30**(4), 325–347 (2020). https://doi.org/10.1007/s00193-019-00927-x
34. Frost, D.L.: Heterogeneous/particle-laden blast waves. Shock Waves **28**(3), 439–449 (2018). https://doi.org/10.1007/s00193-018-0825-1
35. Goring, D.G., Nikora, V.I.: Despiking acoustic doppler velocimeter data. J. Hydraul. Eng. **128**(1), 117–126 (2002). https://doi.org/10.1061/(ASCE)0733-9429(2002)128:1(117)
36. Wahl, T.L.: Discussion of "Despiking acoustic doppler velocimeter data" by Derek G. Goring and Vladimir I. Nikora. J. Hydraul. Eng. **129**(6), 484–487 (2003). https://doi.org/10.1061/(ASCE)0733-9429(2003)129:6(484)
37. Mori, N., Suzuki, T., Kakuno, S.: Noise of acoustic doppler velocimeter data in bubbly flows. J. Eng. Mech. **133**(1), 122–125 (2007). https://doi.org/10.1061/(ASCE)0733-9399(2007)133:1(122)
38. Gurney, R.W.: The initial velocities of fragments from bombs, shell, and grenades. Technical report, Aberdeen Proving Ground, Ballistic Research Laboratory, Wright Field, Dayton, Ohio (1943)
39. Milne, A.M.: Gurney analysis of porous shells. Propellants Explos. Pyrotech. **41**(4), 665–671 (2016). https://doi.org/10.1002/prep.201600016
40. Loiseau, J., Pontalier, Q., Milne, A.M., Goroshin, S., Frost, D.L.: Terminal velocity of liquids and granular materials dispersed by a high explosive. Shock Waves **28**(3), 473–487 (2018). https://doi.org/10.1007/s00193-018-0822-4
41. Frem, D.: Estimating the metal acceleration ability of high explosives. Def. Technol. **16**(1), 225–231 (2020). https://doi.org/10.1016/j.dt.2019.07.002